Research articles

# Structure and magnetic properties of the $Co_{1-x}Ni_xFe_2O_4$-$BaTiO_3$ core-shell nanoparticles

U. Salazar-Kuri [a,*], J.O. Estevez [b], N.R. Silva-González [a], U. Pal [a], M.E. Mendoza [a]

[a] *Instituto de Física, Benemérita Universidad Autónoma de Puebla, Apdo. Postal J-48, Puebla, Pue. 72570, Mexico*
[b] *Departamento de Materia Condensada/Instituto de Física UNAM, Circuito de la Investigación Científica, Ciudad Universitaria, C.P. 04510, Mexico*

## ARTICLE INFO

## ABSTRACT

Core-shell $Co_{1-x}Ni_xFe_2O_4$-$BaTiO_3$ ($0 \leq x \leq 1$) composite nanoparticles were synthetized by a combination of soft chemical routes such as co-precipitation and sol gel. X-ray diffraction patterns confirm the presence of both the materials, the ferrite solid solution, and $BaTiO_3$. Unit cell parameters become smaller as Ni concentration is increased. SEM and HRTEM micrographs corroborate the formation of core-shell nanostructures. Magnetic behaviors of the core are very different from those of the composites. Anomalous magnetic behavior of the composite nanostructures have been discussed considering a coupling between the ferromagnetic and ferroelectric phases. Present work provides an experimental evidence of complex behaviors in magnetoelectric composites and strengthens the idea of remarkable changes of the magnetoelectric properties depending on the nanostructures, morphology or the method of synthesis.

## 1. Introduction

Composites of spinel type structures such as $CoFe_2O_4$ with $BaTiO_3$ have been reported to exhibit magnetoelectric (ME) coupling [1–3]. ME coupling effect is the phenomenon of inducing magnetic polarization by applying an external electric field or an electric polarization by applying an external magnetic field. The effect is due to the mechanical coupling of the piezoelectric and magnetostrictive phases, i.e., when a magnetic field is present, magnetostriction in the spinel phase results in mechanical stresses that are transferred to the piezoelectric phase in the ferroelectric material, giving rise to an electric polarization [4]. Similar phenomenon occurs when piezoelectric material is present and electric field, provoking the magnetic polarization in the magnetostrictive phase.

The idea of preparing composites where the individual magnetic and electric properties of the components are preserved is very important to obtain materials with strong ME coupling due to their promising applications in devices such as in spintronics and MERAMS. Several composites have been identified as magnetoelectric materials [5–9], including nickel cobalt ferrite nanoparticles in a barium strontium titanate matrix [10] or cobalt ferrite nanopillars embedded in ferroelectric barium titanate matrix to generate in-plane electric polarization [11]. However, the understanding of the ME coupling process in composite nanostructures is far from complete. Raidonga et al. [12] analyzed the magnetic and dielectric properties of different core-shell nanostructures of $CoFe_2O_4$-$BaTiO_3$ to explore the ME effect, finding a remarkable change of the magnetocapacitance in different composite nanostructures.

Cobalt ferrite ($CoFe_2O_4$) belongs to the spinel ferrites with general formula $\{(A^{+2})[B_2^{+3}]O_4^{-2}\}$, where, $A^{+2}$ and $B^{+3}$ cations occupy tetrahedral and octahedral interstitial sites of a FCC lattice formed by the oxygen ions. $CoFe_2O_4$ has been extensively studied due to its high saturation magnetization and coercivity which make it a promising hard magnetic material for different applications [13], such as ferrofluids, color imaging, high frequency devices, recording, etc. However, for other practical applications such as biomedical applications, it is necessary to tailor its magnetic properties to achieved low coercivity or low magnetic saturation [14]. From this point of view, properties of magnetic ferrites change drastically as a function of particle size, morphology [15] or by the addition of nickel in cobalt ferrites [14]. On the contrary, nickel ferrite ($NiFe_2O_4$), is a soft magnetic material with inverse spinal structure in the bulk form, i.e., divalent atoms such as $Ni^{+2}$ occupy octahedral [B] sites, while trivalent atoms $Fe^{+3}$ are equally distributed among A and B sites.

Magneto-electric composite nanoparticles, such as, $CoFe_2O_4$-$BaTiO_3$ have been used as field-controlled high-specificity targeted

* Corresponding author.
  *E-mail address:* usalazar@ifuap.buap.mx (U. Salazar-Kuri).

drug delivery systems to eradicate ovarian cancer [16]. The chemical and mechanical stability, along with cytotoxic behaviors of $CoFe_2O_4$ and $BaTiO_3$, which are very important factors for their environment and biomedical applications have been investigated [17].

Motivated by these results, we considered to synthesized $Co_{1-x}Ni_xFe_2O_4$-$BaTiO_3$ (0 < x < 1) composites to study their structure and magnetic properties as function of nickel content. Low temperature soft chemical routes have been used to synthesize the composites in order to preserve the core-shell structure of the nanoparticles and guarantee the multiferroic interactions at nanoscale.

## 2. Materials and methods

### 2.1. Synthesis of $Co_{1-x}Ni_xFe_2O_4$ nanoparticles

Synthesis of $Co_{1-x}Ni_xFe_2O_4$ nanoparticles was performed by co-precipitation following the procedure reported by Duong et al. [18]. Stoichiometric amounts of cobalt nitrate hexahydrate Co $(NO_3)_2 \cdot 6H_2O$, nickel nitrate hexahydrate $Ni(NO_3)_2 \cdot 6H_2O$ and iron nitrate nonahydrate $Fe(NO_3)_3 \cdot 9H_2O$ were dissolved in deionized water. The solution was heated to 70 °C and then a sodium hydroxide solution (NaOH 2.05 M), was added to it slowly under continuous mechanical stirring at 1000 rpm. The mixture was left for one hour at 70 °C. After a free cooling to room temperature, the precipitate was separated and washed with deionized water several times (until the pH reached to 7) and then dried at 80 °C for 12 h, to obtain it in powder form. All the as-prepared samples were calcined in air at 500 °C for 1 h.

### 2.2. Synthesis of $Co_{1-x}Ni_xFe_2O_4$-$BaTiO_3$ core-shell composites

$Co_{1-x}Ni_xFe_2O_4$-$BaTiO_3$ composites were prepared through the sol-gel route [4]. 0.116 g of barium carbonate ($BaCO_3$) and 0.4 g of citric acid were dissolved in 120 ml of deionized water and mixed with 120 ml of an ethanolic solution of 4.0 g of citric acid and 0.192 ml of titanium isopropoxide. 0.1 g of $Co_{1-x}Ni_xFe_2O_4$ powder was dispersed in the mixed solution under vigorous sonication for 1 h. After the sonication, the mixture was dried at 80 °C overnight and subsequently calcined at 780 °C for 5 h to get powder of $Co_{1-x}Ni_xFe_2O_4$-$BaTiO_3$.

### 2.3. Characterization of the samples

The phase identification of solid solution, barium titanate and composites were performed by powder X-ray diffraction (XRD) using a PANalytical X-ray Empyrean diffractometer with Cu-K$_\alpha$ radiation ($\lambda$ = 1.5406 Å) at 45 kV and 40 mA. Lattice parameters were refined using High Score Plus 3.1 package. Morphology of the single phase and core-shell nanostructures were investigated utilizing a Jeol JSM-7800F field emission scanning electron microscope and a Jeol JEM-2010F high resolution transmission electron microscope (HRTEM). Elemental analyses of samples were performed using an Oxford Instrument X-Max spectrometer coupled to the JSM-7800F. Magnetic measurements of the samples were performed using a Dynacool-9 physical properties measurement system (PPMS) of Quantum Design. For magnetic characterization, the magnetization vs. magnetic field hysteresis loops of the powder samples were recorded at room temperature up to 1.5 T, and their field cooling (FC) and zero field cooling (ZFC) curves were recorded under 100 Oe applied field between 20 and 375 K.

## 3. Results and discussion

Fig. 1 shows the XRD patterns of the annealed powder samples synthesized by co-precipitation technique. The final products correspond to a solid solution of $Co_{1-x}Ni_xFe_2O_4$. The pure $CoFe_2O_4$ (x = 0) and $NiFe_2O_4$ (x = 1) correspond to the spinel structure of the desired ferrites. Revealed diffraction peaks are consistent with the reported data for spinel ferrites (PDF cards # 22-1086 for $CoFe_2O_4$ and # 74-2081 for $NiFe_2O_4$), indicating that powders are in single solid solution phase $Co_{1-x}Ni_xFe_2O_4$ without any other phases or impurities. Fig. S3.

Average crystallite sizes (D) of the samples were calculated from the most intense (3 1 1) peak using Scherrer's equation [19]:

$$D = \frac{0.9\lambda}{\beta_{1/2}\cos\theta}$$

where $\lambda$, $\beta_{1/2}$ and $\theta$ are the X-ray wavelength, full width at half maximum (FWHM) of the diffraction peak, and its Bragg diffraction angle, respectively. The value 0.9 corresponds to the shape factor for spherical crystallites. In general crystallite size varies from 20.36(1) for x = 0 to 13.92(2) for x = 1. Table 1 presents the refined values of the lattice parameter for the solid solution $Co_{1-x}Ni_xFe_2O_4$. $R_{wp}$ range for the refinement calculation was between 2.5 and 9.6.

Lattice parameter a reduces as the nickel concentration increases due probably to the smaller radius difference between $Ni^{2+}$ (0.72 Å) and $Co^{2+}$ (0.74 Å), in agreement to the calculations reported by H. Y. He for their hydrothermally prepared nanoparticles [20].

The room temperature XRD patterns of the composites $Co_{1-x}Ni_xFe_2O_4$-$BaTiO_3$ (CNFO-BTO) after sol-gel synthesis and calcination at 780 °C for 5 h are given in Fig. 2. Well-defined diffraction peaks in the XRD patterns of the composite samples revealed the presence of $Co_{1-x}Ni_xFe_2O_4$ in solid solution phase, and $BaTiO_3$ in tetragonal phase (PDF 077-4195). No additional peaks were observed either from impurities or intermediate phases confirming the successful formation of the composites.

Typical morphologies of $CoFe_2O_4$ (CFO) and $NiFe_2O_4$ (NFO) powder samples after annealing at 500 °C are presented in Fig. 3. As can be seen from the micrographs, the samples consist of agglomerated semi-spherical particles (even for the solid solution not shown here) of 10–35 nm sizes with average size (c.a.) 21.9 nm, and 16.0 nm, for CFO and NFO, respectively. There are size regimes for different magnetic materials in which there exists a transition from multi-domain to single-domain, which is energetically favorable for the magnetic grains (or particles) to exist without domain wall [21,22], which probably also depends on their shapes [23]. However it is difficult to find the critical size. As the reported size range for our solid solution is >12 nm for occurring such transition, we expect "pseudo-single domain" structures for our nanoparticles [24,25] due to their spherical shapes.

Elemental analysis of the samples was performed by energy dispersive spectroscopy (EDS). Table 2 presents the quantitative estimation of Co, Ni, Fe and O in each of the solid solutions $Co_{1-x}Ni_xFe_2O_4$. It can be noticed that for all the samples, the experimental atom percentages of the metals are lower than their nominal values, probably due to the used synthesis method, where a fraction of metal ions remain in the reaction solution, and it was lost during the repeated washing of the precipitate. The difference is more significant for Ni percentage. The nickel content in the solid solution remained always lower than its nominal value due to the loss of Ni ions that remains in the solution [26].

The morphology of the synthesized cobalt and nickel ferrites were studied further through TEM analysis. From the typical TEM and HRTEM images presented in Fig. 4 a–d, we can perceive the near-spherical morphology of the ferrite nanoparticles. The
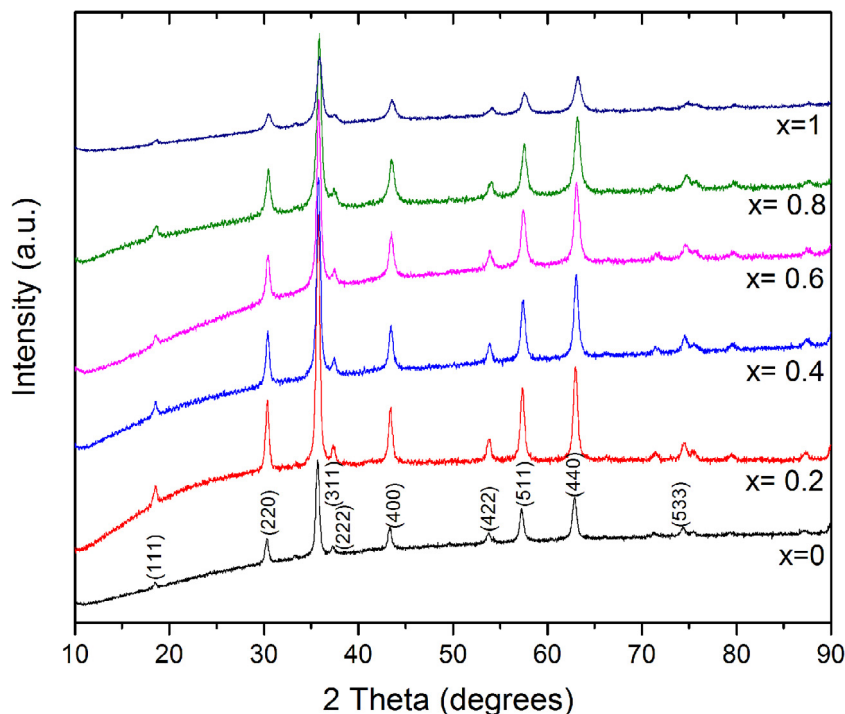
**Fig. 1.** XRD patterns of the annealed (500 °C 1 h) $Co_{1-x}Ni_xFe_2O_4$ powders (x = 0, 0.2, 0.4, 0.6, 0.8, 1) prepared by co-precipitation route. Diffraction peaks were indexed considering PDF file 22-1086.

**Table 1**
Composition and refined lattice parameter of $Co_{1-x}Ni_xFe_2O_4$.

| Composition, x | Lattice parameter a (Å) |
|---|---|
| 0.0 | 8.385(1) |
| 0.2 | 8.365(7) |
| 0.4 | 8.359(1) |
| 0.6 | 8.354(1) |
| 0.8 | 8.343(9) |
| 1.0 | 8.341(2) |

average particle sizes estimated from TEM images were 21.6 and 14.6 nm for CFO and NFO, respectively. As can be noticed, these TEM estimated average sizes are smaller than those calculated from the SEM micrographs of the samples. Typical TEM images of the solid solution structures of x = 0.2, 0.4, 0.6 and 0.8 are presented in Fig. S1 (supplementary information). A reduction of particle size and enhancement in particle agglomeration with the increase of Ni concentration can be observed from the micrographs. On the other hand, the morphology of the $BaTiO_3$ (BTO) nanoparticles prepared by sol-gel method and annealed at 780 °C for 5 h are non-spherical (Fig. 4 e, f). The size of these BTO particles vary between 53 and 95 nm, quite bigger than the ferrites. HRTEM micrographs of CFO, NFO and BTO are shown in Fig. 4b, d and f, respectively. Crystallographic behaviors of the fabricated nanostructures were identified by measuring the interplanar spacing, d, using the software digital micrograph 3.7.0. Fig. 4b presents a 35 nm well crystalline $CoFe_2O_4$ particle with defect free stacked (1 1 1) crystalline planes. However, in the case of $NiFe_2O_4$, the particles are multigrain structures, oriented along (3 1 1) and (2 2 0) planes (Fig. 4d). Fig. 4f shows two crystallographic planes of BTO, (1 0 0) and (1 0 1).

Typical TEM images of the CFO-BTO, NFO-BTO and CNFO-BTO with x = 0.2 nanoparticles are presented in Fig. 5. From the low resolution TEM images of these samples (left column, Fig. 5 a, c, and e) we can see a poor particle dispersion in the samples, frequently

forming bigger aggregates of several particles, the formation of core-shell structures in the samples can still be appreciated from the contrast differences in their local structures (shown by arrows). For all the samples, the average particle size is larger than the average particle size of their core particles. For example, the average particles sizes were 27.6, 22.4 nm, and 27 nm for the CFO-BTO, NFO-BTO, and $Co_{0.8}Ni_{0.2}Fe_2O_4$-$BaTiO_3$, respectively, which are larger than corresponding core particles of average sizes of 21.6, 14.6, and 20.9, respectively. As has been stated earlier, Ni incorporated alloy structures induce higher agglomeration of the formed nanoparticles, causing the formation of bigger core-shell structures, frequently encapsulating more than one particles in the core (Fig. 5e). As expected, the HRTEM images (Fig. 5b, d, and e) of the samples did not reveal dispersed core-shell structures. However, the formation of crystalline BTO layers around CFO, NFO, and CNFO core particles is clear from their characteristic lattice fringes correspond to (1 0 1), (0 0 2) and (1 1 0) planes. Typical TEM images of the core-shell particles with composite cores (x = 0.2, 0.4, 0.6 and 0.8) are presented in Fig. S2 of the supplementary information.

To verify the formation of core-shell structures in the composite nanoparticles, we performed their elemental mapping in a Jeol JSM-7800 F field emission scanning electron microscope. The mapping images of the samples are presented in Fig. S3 of the supplementary information. While due to particle agglomeration in the samples and resolution restriction of the EDS mapping system, it was not possible to reveal the core-shell nature of the composite particles, as can be perceive from the images (Fig. S3). However, the intensities of Ba and Ti signals in all the samples, emanating from BTO, are stronger than the signals of Co, Ni and Fe for all the samples, suggesting the formation of the core-shell structures in them.

The room temperature magnetization (M) vs magnetic field (H) plots the solid solution $Co_{1-x}Ni_xFe_2O_4$ used as ferrite core are depicted in Fig. 6. For the sake of clarity, the saturation magnetization $M_S$ and coercive field $H_C$ as function of doping concentration (x) are presented as inset of Fig. 6. As can be seen, both $M_S$ and
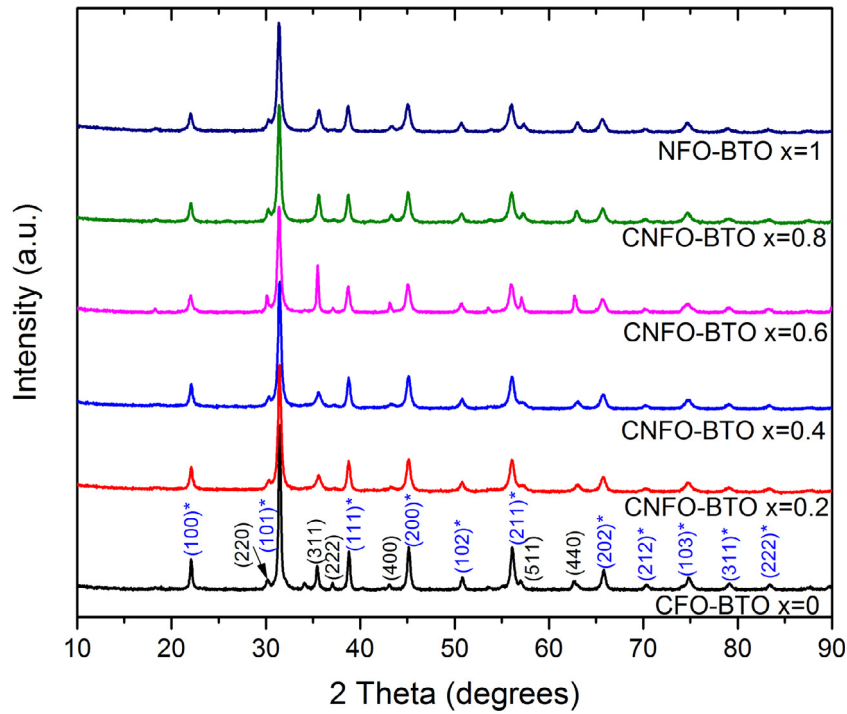
**Fig. 2.** XRD patterns of the composites $Co_{1-x}Ni_xFe_2O_4/BaTiO_3$ (CNFO-BTO). The peaks indexed in black are the peaks associated to the spinel phases and peaks indexed in blue (with asterisk) correspond to the planes associated to the $BaTiO_3$ phase.
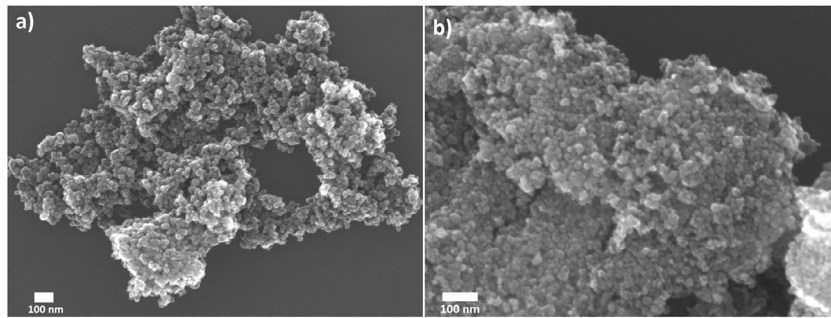


**Fig. 3.** Typical SEM micrographs of a) $CoFe_2O_4$ and b) $NiFe_2O_4$ nanoparticles.

**Table 2**
Experimental and nominal values of the atomic percentage contents of different elements in the solid solution $Co_{1-x}Ni_xFe_2O_4$.

| Element | Exp. | Nom. | Exp. | Nom. | Exp. | Nom. | Exp. | Nom. | Exp. | Nom. | Exp. | Nom. |
|---------|------|------|------|------|------|------|------|------|------|------|------|------|
| | x = 0 | | x = 0.2 | | x = 0.4 | | x = 0.6 | | x = 0.8 | | x = 1 | |
| Co | 13,12 | 14.28 | 11.36 | 11.42 | 8.72 | 8.57 | 4.93 | 7.71 | 3.27 | 2.86 | 0 | 0 |
| Ni | 0 | 0 | 2.49 | 2.86 | 5.12 | 7.71 | 6.83 | 8.57 | 10.73 | 11.42 | 11.75 | 14.28 |
| Fe | 26.27 | 28.57 | 27.27 | 28.57 | 27.27 | 28.57 | 23.05 | 28.57 | 28.68 | 28.57 | 26.22 | 28.57 |
| O | 60.61 | 57.14 | 58.88 | 57.14 | 58.64 | 57.14 | 65.19 | 57.14 | 57.31 | 57.14 | 62.00 | 57.14 |

$H_C$ decreases with the increase of Ni fraction (x). Such decrease of saturation magnetization and coercivity has also been observed for mixed ferrites and attributed to the smaller magnetic moment of $Ni^{+2}$ at the octahedral sites in comparison with $Co^{+2}$ [15,27,28]. Maaz et al. [15] also reported the lower values of magnetization of nanoparticles with respect to their bulk values (differences of about ~33.7 emu/g for $NiFe_2O_4$ and ~15 emu/g for $CoFe_2O_4$). They attributed this behavior to the existence of spin glass structure that inhibits the spins to align along the field direction, causing a reduced magnetization. Presence of impurities in the form of Co- or Ni-oxides, which are antiferromagnetic in nature, can also

reduce the magnetization of mixed ferrites. EDS analysis of our mixed ferrite structures revealed a deficient atomic percentage of Ni, provoking Ni vacancies ($V_{Ni}$) within the structures. Those Ni vacancies might also be responsible for the reduction of $M_s$ in our ferrite nanoparticles. However, unlike the observation of Maaz et al. [15] we did not encounter any unindexed peak in the XRD pattern of $NiFe_2O_4$ (x = 1). On the other hand, the Co content discrepancy measured by EDS with respect to theoretical values is lower, so the magnetization has a lower discrepancy than from its bulk value (~15 emu/g). It is also well known that annealing at higher temperature improves crystallinity of polycrystalline
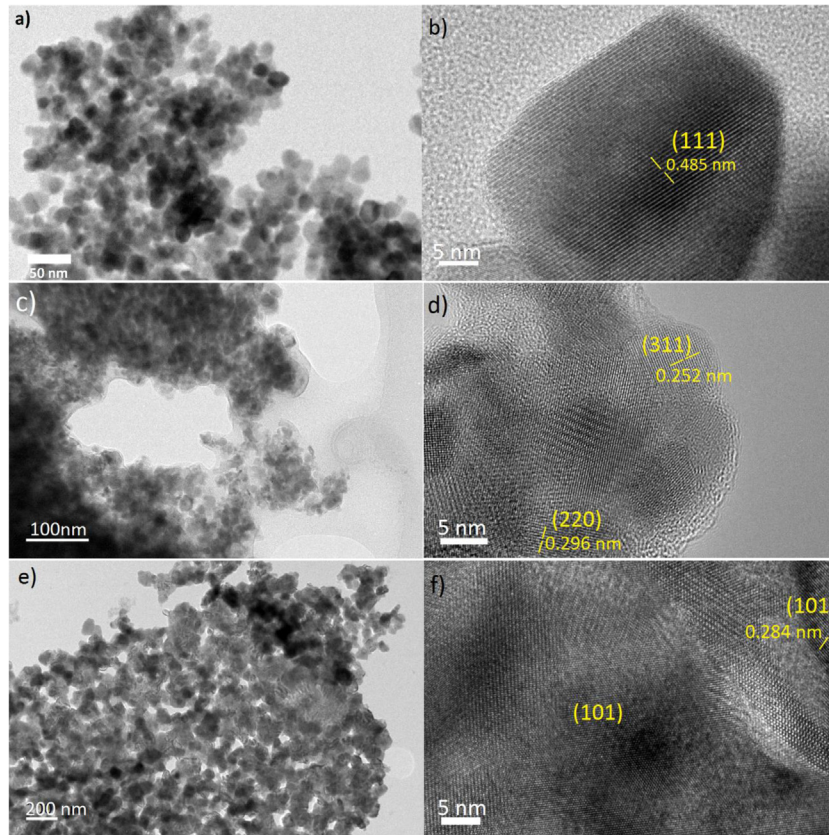
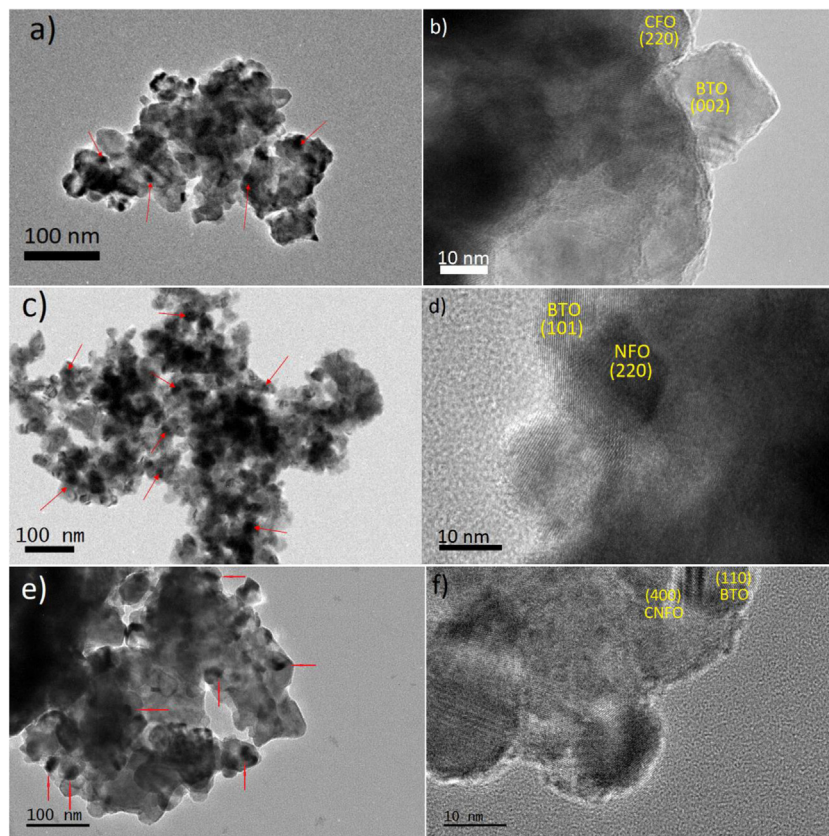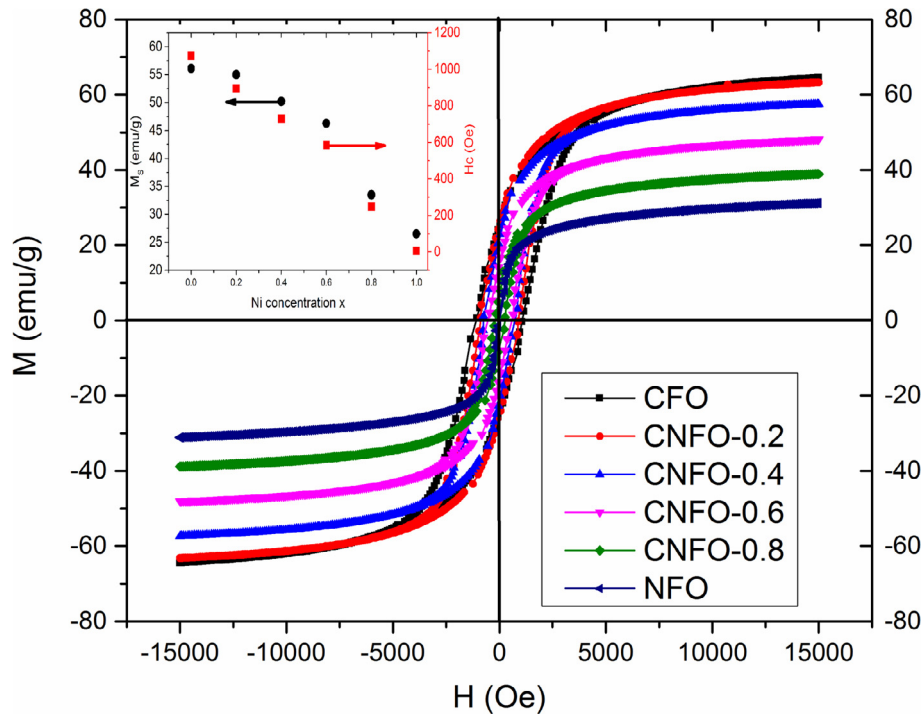**Fig. 4.** Typical TEM and HRTEM micrographs for a) and b) CFO, c and d) NFO, and e) and f) BTO.



**Fig. 5.** Typical TEM and HRTEM images of the a)-b) CFO-BTO and c)-d) NFO-BTO and e)-f) CNFO-BTO with x = 0.2. Arrows indicate the formation of core-shells.

**Fig. 6.** Magnetization hysteresis loops for $Co_{1-x}Ni_xFe_2O_4$ (where x = 0, 0.2, 0.4, 0.6, 0.8, 1) at room temperature up to a maximum applied field of 15 kOe. Inset shows the variation of spontaneous magnetization $M_s$ and coercivity $H_C$ as function of Ni concentration.

materials. However, it also increases the grain size, affecting their magnetic properties [1,29,30]. In order to avoid the growth of crystallite size, Shi et al. proposed a synthesis technique combining co-precipitation and mechanical alloying, obtaining nanoparticles of 10 nm size for both: $CoFe_2O_4$ [28] and $NiFe_2O_4$ [26]. As has been mentioned earlier, this size belongs to the regime of pseudo single domain magnetic structures, and hence the particles revealed almost zero coercive field and high $M_S$ values. On the other hand, other synthesis methods such as low-temperature auto-combustion [31], rheological phase reaction [4] and solid state reaction [32] produced nanoparticles in the 23 to 70 nm size range, depending on the temperature and time of reaction. Saturation magnetization and coercive field are also seen to be dependent on the synthesis method and annealing temperature [30,31,33]. Therefore, as suggested by S. Xiao et al. [31], the low temperature techniques such as sol-gel and co-precipitation are the best synthesis procedures for the production of high-quality uniform particles at low temperature and low cost, with acceptable magnetic properties, depending on the applications they are aimed to.
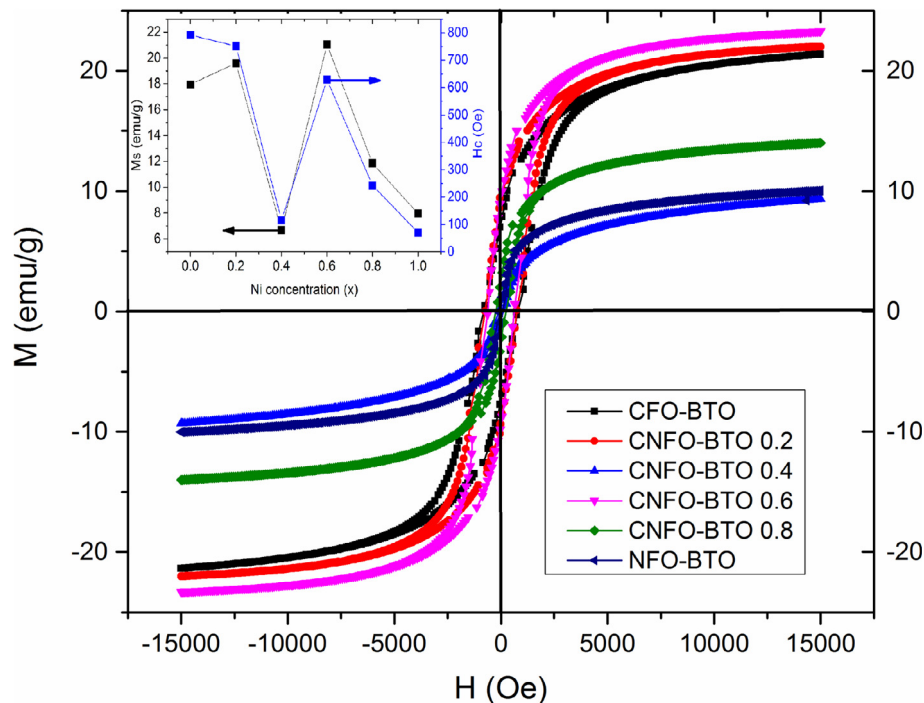
Fig. 7 shows the magnetization hysteresis loops for the composite CNFO-BTO as function of Ni concentration at room temperature. Variations of $M_S$ and $H_C$ with Ni concentration of magnetic core are depicted as inset. In general BTO coated composites revealed lower $M_S$ and $H_C$ values due to the diamagnetic character of BTO, affecting the magnetic moment of the composite by changing the distribution of ions and their spin orientations [34,35]. As can be seen from inset of Fig. 7, the variations of $M_S$ and $H_C$ for the samples of core-shell structures with Ni concentration are very different from the variations observed for mixed ferrites (inset of Fig. 6). The composites core-shell structures show anomalous variations of $Ms$ and $Hc$ especially for x = 0.2, 0.4 and 0.6. As mentioned in the introduction, the idea of preparing these composites is to induce a ME coupling via a magnetic or electric polarization with the application of an external electric or magnetic field due to the mechanical coupling of the piezoelectric and magnetostrictive phases. The results presented in Fig. 7 indicate that the composite provokes an anomalous

interaction between these two phases for intermediate Ni concentrations of the ferrite, due probably to this strong mechanical interaction between the two phases.

The ZFC and FC magnetization curves of the ferrite and core-shell samples measured in between 20 and 350 K under 100 Oe applied magnetic field are presented in Fig. 8. The ZC and FC curves of the $Co_{1-x}Ni_xFe_2O_4$ solid solutions (Fig. 8a) revealed a large divergence for x = 0 to 0.6. The divergence increases with the decrease of temperature. Furthermore, their ZFC curves have higher magnetizations than the FC curves. This unusual behavior has been observed in manganite $La_{0.275}Pr_{0.35}Ca_{0.375}MnO_3$ [36] and was associated to the large magnetostriction of the material [37], i.e., any change in spin direction results in large orbital orientation associated to magnetocrystalline anisotropy with high coercive fields [29,38]. The effect is very clear for the solid solution structures (Fig. 6), where the coercive fields are high for lower x values, indicating a gradual transition of magnetic behavior of the alloy from hard to soft magnetic with the increase of Ni content.

For the Ni concentration x = 0.8, the ZFC and FC curves converge at lower temperatures, and finally for x = 1 ($NiFe_2O_4$), they flip over (FC curve a top of the ZFC curve). The maximum of ZFC curve is generally associated with the superparamagnetic blocking temperature ($T_B$). Considering this peak in the ZFC curves, the estimated $T_B$ was found to be around 305 K for all the solid solution (x = 0.0 to x = 0.8) ferrites, the value which match with the reported $T_B$ value of 12 nm particles of $CoFe_2O_4$ [39] indicating that the hard magnetic $CoFe_2O_4$ dominates over the soft magnetic $NiFe_2O_4$. Nickel ferrite (x = 1) has a $T_B$ around 275 K, consistent with the $M$-$H$ curve measured at room temperature and showing no coercive field.

In general, the $M$ values of the CNFO-BTO samples are lower than the solid solution ferrites due to the presence of the BTO shell. As observed in the hysteresis loops (Fig. 7), composite formation induces anomalous behavior (no particular pattern) in their magnetization. For x = 0.0, 0.2 and 0.6, there is a divergence between the ZFC and FC curves at lower temperatures, and ZFC curve remain

**Fig. 7.** Ferromagnetic hysteresis loops for the composite CNFO-BTO at room temperature up to a maximum applied field of 15 kOe. Inset shows the spontaneous magnetization *Ms* and coercivity *Hc* as function of Ni concentration.
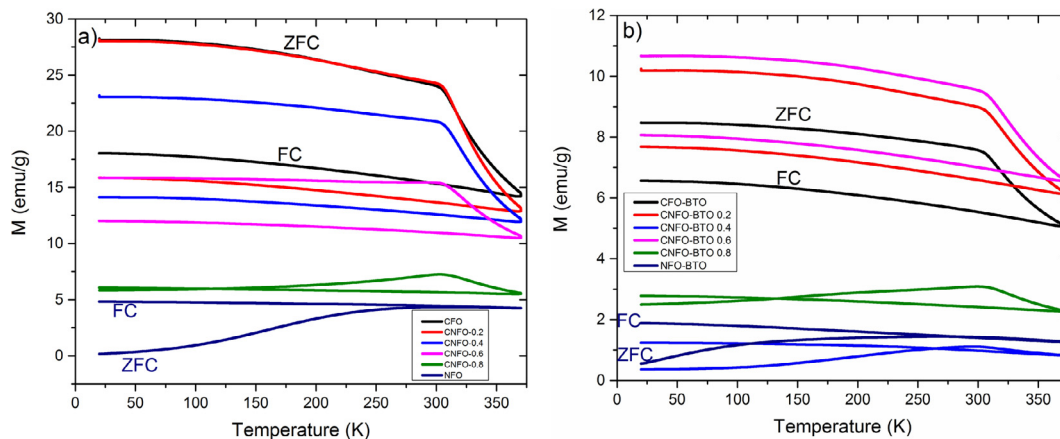


**Fig. 8.** ZFC and FC plots for the a) solid solution $Co_{1-x}Ni_xFe_2O_4$ and b) CNFO-BTO composites (x = 0, 0.2, 0.4, 0.6, 0.8, 1) recorded under 100 Oe applied magnetic field.

a top of the FC curve. For x = 0.4, there is also a divergence between ZC and FC curves. However, the ZFC curve remains below the FC curve at low temperatures. While the $T_B$ of the solid solution ferrites remains around 305 K, irrespective of composition x, for x = 1 (NFO-BTO) the $T_B$ is around 245 K, indicating the influence of BTO shell in the magnetic properties of solid solution ferrites. Chaudhuri et al. [4], and Raidongia et al. [12] measured the ZFC and FC curves for $CoFe_2O_4$-$BaTiO_3$ core-shell composites, reporting contradictory results, which are also different from the results obtained in the present study. We must note that while Chauduri et al. [4] prepared core-shell spherical-type composite nanostructures by hydrothermal method, followed by a sol-gel method to obtain particles of around 20 nm diameter, Raidongia et al. prepared core-shell nanotubes by a combination of solution processing and high temperature calcination. The results obtained by them indicate the magnetic properties of both the solid solution ferrites and core-shell multiferroic nanostructures depend strongly

to the adopted method of their synthesis, their sizes and morphology. On the other hand Grössinger et al. [40] measured the magnetization curves of their core-shell composites as a function of temperature, and also observed that the heating curve (ZFC) remain a top of the cooling curve (FC) with a decrease in magnetization with the increase of temperature. They attributed this behavior to the breakdown of the alignment of the electric dipoles in BTO and to the different degree of alignment of these electric dipoles when cooling. We believe, the same effects are responsible for the anomalous magnetic behaviors of the core-shell composite multiferroic nanostructures fabricated in the present work. In fact, different behaviors have been observed in multiferroic composites depending on the nature, method of synthesis, and morphology of the particles. Anomalous magnetic and magnetodielectric behaviors of multiferroic composites and the effect of interfaces have been summarized by Acevedo et al. [41] for different ferrites including BTO-BTO, BTO-CFO and CFO-CFO systems.

## 4. Conclusion

Multiferroic core-shell $Co_{1-x}Ni_xFe_2O_4$-$BaTiO_3$ ($0 \leq x \leq 1$) composites were successfully synthesized by a combination of co-precipitation and sol-gel techniques. While in general, the magnetic behavior of solid solution ferrite cores vary systematically in between $CoFe_2O_3$ and $NiFe_2O_3$, the multiferroic core-shell structures present an anomalous behavior in the magnetization for $x = 0.2$ to $0.6$ due to the magnetoelectric coupling of the nanoparticles which triggers complex phenomena that need further understanding.

## Appendix A. Supplementary data

Supplementary data associated with this article can be found, in the online version, at http://dx.doi.org/10.1016/j.jmmm.2017.06.126.

## References

[1] G.V. Duong, R. Groessinger, J. Magn. Magn. Mater. 316 (2007) e624.
[2] V. Giap, R. Grössinger, R. Sato-Turtelli, J. Magn. Magn. Mat. 310 (2007) e361.
[3] G. Evans, G.V. Duong, M.J. Ingleson, Z. Xu, J.T.A. Jones, Y.Z. Khimyak, J.B. Claridge, M.J. Rosseinsky, Adv. Func. Mat. 20 (2010) 231.
[4] A. Chaudhuri, K. Mandal, J. Magn. Magn. Mater. 377 (2015) 441.
[5] V. Corral-Flores, D. Bueno-Baqués, R.F. Ziolo, Acta Mater. 58 (2010) 764.
[6] G. Sreenivasulu, M. Popov, F.A. Chavez, S.L. Hamilton, P.R. Lehto, G. Srinivasan, Appl. Phys. Lett. 104 (2014) 052901.
[7] P.N. Oliveira, D.M. Silva, G.S. Dias, I.A. Santos, L.F. Cótica, Ferroelectrics 499 (2016) 76.
[8] P.N. Oliveira, D. Alanis, R.D. Bini, D.M. Silva, G.S. Dias, I.A. Santos, L.F. Cótica, R. Guo, A.S. Bhalla, Integr. Ferroelectr. 174 (2016) 88.
[9] Q. Yang, W. Zhang, M. Yuan, L. Kang, J. Feng, W. Pan, J. Ouyang, Sci. Technol. Adv. Mater. 15 (2014) 025003.
[10] P. Pahuja, R. Sharma, V. Singh, R. Pal Tandon, Int. J. Appl. Ceram. Technol. 12 (2015) 156.
[11] C. Schmitz-Antoniak, D. Schmitz, P. Borisov, F.M.F. de Groot, S. Stienen, A. Warland, B. Krumme, R. Feyerherm, E. Dudzik, W. Kleemann, H. Wende, Nat. Commun. 4 (2012) 2051.
[12] K. Raidonga, A. Nag, A. Sundaresan, C.N.R. Rao, Appl. Phys. Let. 97 (2010) 062904.
[13] X. Meng, H. Li, J. Chen, L. Mei, K. Wang, X. Li, J. Magn. Magn, Mater. 321 (2009) 1155.
[14] V.L. Mathe, A.D. Sheikh, Phys. B. Condens. Matter 405 (2010) 3594.
[15] K. Maaz, W. Khalid, A. Mumtaz, S.K. Hasanain, J. Liu, J.L. Duan, Phys. E 41 (2009) 593.
[16] R. Guduru, P. Liang, C. Runowicz, M. Nair, V. Atluri, S. Khizroev, Sci. Rep. 3 (2013) 2953.
[17] M.M. Eshaghian-Wilner, A. Prajogi, K. Ravicz, G. Sarkar, U. Sharma, R. Guduru, S. Khizroev, Chapter in wireless Computing in Medicine: From Nano to Cloud with Ethical and Legal Implications, Wiley, 2016, 323.
[18] G.V. Duong, R. Groessinger, R.S. Turtelli, I.E.E.E. Transac Magn. 42–10 (2006) 3611.
[19] J.I. Langford, A.J.C. Wilson, J. Appl. Cryst. 11 (1978) 102.
[20] H.Y. He, J. Appl. Cer. Technol. 11 (2014) 626.
[21] C. Kittel, Rev. Mod. Phys. 21 (1949) 541.
[22] D.J. Craik, D.A. McIntyre, Proc. Phys. Soc., Lond. Sect. A 302 (1967) 99.
[23] E.C. Stoner, E.P. Wohlfarth, Phil. Tans. Roy. Soc., A240, (1948), 599–642, reprint in IEEE Trans. Magn. 27, (1991) 3475–3478.
[24] A.G. Kolhatkar, A.C. Jamison, D. Litvinov, R.C. Willson, T.R. Lee, Int. J. Mol. Sci. 14 (2014) 15977–16009.
[25] K.M. Krishnan, I.E.E.E. Trans, Magn. 46 (2010) 2523.
[26] Y. Shi, J. Ding, X. Liu, J. Wang, J. Magn. Magn. Mat. 205 (1999) 249.
[27] N. Hann, O.K. Quy, N.P. Thuy, L.D. Tung, L. Spinu, Phys. B 327 (2003) 382.
[28] Y. Shi, J. Ding, H. Yin, J. Alloys Compd. 308 (2000) 290.
[29] R. Valenzuela, Cambridge University Press, Cambridge, 1994.
[30] J. Jiang, Y.M. Yang, Mater. Lett. 61 (2007) 4267–4279.
[31] S.H. Xiao, W.F. Jiang, L.Y. Li, X.J. Li, Mater. Chem. Phys. 106 (2007) 82–87.
[32] R.C. Kambale, P.A. Shaikh, S.S. Kamble, Y.D. Kolekar, J. Alloys Compd. 478 (2009) 599–603.
[33] Hai-Yan he, Int. J. Appl. Ceram. Technol. 11 (4) (2014) 626–636.
[34] M.M. Selvi, P. Manimuthu, K.S. Kumar, C. Venkateswaran, J. Magn. Magn. Mat. 369 (2014) 155.
[35] L.P. Curecheriu, M.T. Buscaglia, V. Buscaglia, L. Mitoseriu, P. Postolache, A. Ianculescu, P. Nanni, J. Appl. Phys. 107 (2010) 104106.
[36] B.C. Zhao, Y.Q. Ma, W.H. Song, Y.P. Sun, Phys. Lett. A 354 (2006) 472.
[37] V. Hardy, A. Maignan, S. Hérbert, C. Yaicle, C. Martin, M. Hervieu, M.R. Lees, G. Rowlands, D. Mc, K. Paul, B. Raveau, Phys. Rev. B 68 (2003) 220402.
[38] H. Gavrila, V. Ionita, J. Optoelectr. Adv. Mat. 4 (2) (2002) 173–192.
[39] A.J. Rondinone, A.C.S. Samia, Z.J. Zhang, J. Phys. Chem. B 103 (1999) 6876.
[40] R. Grössinger, G.V. Duong, E. Sato-Turtelli, J. Magn. Magn. Mat. 320 (2008) 1972.
[41] U. Acevedo, R.L. Noda, R. Breitwieser, F. Calderon, S. Ammar, R. Valenzuela, AIP Adv. 7 (2017) 055813.